Shrinkage features, microstructure evolution and properties of Gd_2O_3-MgO optical composite ceramics with Zr as phase stabilizer

Buhao Zhang [a,e], Hetuo Chen [a], Qiangqiang Zhu [b], Zhaomin Yin [b], Peng Liu [c], Junyu Zhang [d], Yutao Liu [a], Run Tian [a], Xiaojian Mao [a]*, Jian Zhang [a], Shiwei Wang [a]*

[a]State Key Laboratory of High-Performance Ceramics and Superfine Microstructure, Shanghai Institute of Ceramics, Chinese Academy of Sciences, Shanghai, 200050, China

[b]College of Optics and Electronic Science and Technology, China Jiliang University, Hangzhou, 310018, China

[c]Jiangsu Key Laboratory of Advanced Laser Materials and Devices, School of Physics and Electronics Engineering, Jiangsu Normal University, Xuzhou, 221116, China

[d]Henan Key Laboratory of Research for Central Plains Ancient Ceramics, Pingdingshan, 467000, China

[e]Faculty of Engineering, University of Nottingham, Nottingham, NG7 2RD, United Kingdom

* Corresponding author.

E-mail: maoxiaojian@mail.sic.ac.cn (X. MAO);

swwang51@mail.sic.ac.cn (S. WANG).

Abstract:

A novel composite ceramic, composed of equal-volumetric Zr-stabilized Gd_2O_3 and MgO phases, was prepared to be transparent in mid-wave infrared range. Zr stabilized Gd_2O_3 is proved to have a lower lattice parameter (10.7516 Å) using XRD refinement. Pressureless sintering behavior of Gd_2O_3-MgO with/without 2 at.% Zr-doping (naming ZGM and GM) was studied via the real-time observation technique. The shrinkage of ZGM green body proceeds steadily up to 1400°C while that of the undoped one shrinks sharply at 1250°C due to Gd_2O_3 phase transition. The segregation of Zr element along the grain boundaries of Zr-Gd_2O_3 creates a synergized effect on the grain refinement with pinning effect. Dense ZGM ceramics exhibit superior transmittance of 78.3%-85.6% at 3-5 μm, which show good consistency with the calculated values. The refractive index of Zr- Gd_2O_3 varies from 1.87 at 3 μm to 1.80 at 5 μm, which is smaller than those of monoclinic Gd_2O_3.

Keywords: Composite ceramic; mid-wave infrared; transparent ceramics; phase transition inhibition.

1 Introduction

Mid-wave infrared (MWIR, 3-5 μm) opto-electric window/dome have been widely used in high-speed vehicles, owing to their sophisticated structures and clear objectives [1]. Hot-pressed MgF_2 [2] and Y_2O_3 [3], as common MWIR transparent materials, possess farther IR edge than $MgAl_2O_4$ [4] and AlON [5] transparent ceramics. However, once the vehicles approaching the hypersonic speed, they would become less competitive due to the pronounced ceiling effect in mechanical properties.

Composite ceramics are proposed to solve the present puzzle by incorporating a secondary phase, together with transparentizing in the infrared range. Novel biphasic optical composite ceramics have attracted attention that good optical performance in MWIR range and promising mechanical properties were demonstrated [6]. Based on the Mie scattering theory, the high MWIR transmittance of composite requires that grain size must be substantially smaller than the wavelength of incident light to reduce

optical scatter to tolerable levels. MgO, possessing outstanding IR cut-off at ~10 μm [7], was selected as the Zener pinning phase within rare earth oxides (RE_2O_3) matrix [8]. The Zener effect is insufficient to produce nanometric composite ceramics when using pressureless sintering. Although the smaller particle sizes, the higher the Zener drag and pinning among biphasic phase boundary impingement. However, grain growth of nanosized Y_2O_3 and MgO will inevitably happen in the form of agglomerates at the early stage of sintering [9]. Most of the Y_2O_3-MgO related research works were reported densified by means of pressure-assisted sintering techniques. Harris et al. reported that ~80% infrared transmittance of hot-pressed Y_2O_3–MgO composite ceramics was successfully obtained at 4-6 μm [10]. The thermal shock resistance parameter was twice higher than that of common 3–5 μm window materials. Liu et al. [11] fabricated the MWIR transparent Y_2O_3–MgO nanocomposites with transmittance up to 64.5% at 1.6 μm owing to the 300 MPa pressure-assisted spark plasma sintering (SPS) at a relatively lower sintering temperature. The hardness and fracture toughness also increased owing to the crack deflecting, bridging and branching toughening mechanisms [12].

Gd_2O_3, a more universal RE_2O_3 with low phonon energy and good irradiation resistance, is expected to further improve structural and functional performance of its composite ceramics. It has recently been reported to mix Gd_2O_3 with MgO via hot-pressing (HP) sintering at 1250°C-1350°C under a uniaxial pressure of 60 MPa in Li et al 's work [13]. The hot-pressed Gd_2O_3-MgO composite ceramic showed good transparency (67.3 %-84.7 % at 1.4-6 μm), and a high hardness of 14.3 ± 0.2 GPa, which was ascribed to the uniaxial pressing [14]. The excellent properties were mainly resulted from the pressure-assisted grain refinement with the final grain size <100 nm. More importantly, the use of hot-pressed graphite dies led to a typical loss in transmittance at around 7 μm [15, 16]. The hybrid of mould-free pressureless pre-sintering and HIP tactic can be more practical and competitive to densify Gd_2O_3-MgO composite ceramic with promising advantages in manufacturing cost, the scale-up process and free shaping into complex bodies [17, 18].

Noticeably, the phase transition of Gd_2O_3 from cubic to monoclinic crystalline structure happened at around 1250°C [19], which has a negative effect on the pressureless pre-sintering of Gd_2O_3-MgO composite ceramic. A sharp volume shrinkage up to 10% will happen due to the phase transition and induce crack formation in the green bodies. It is of great significance to stabilize the cubic crystal structure of Gd_2O_3 in the Gd_2O_3-MgO biphasic system. It can be inferred from the Gd_2O_3-ZrO_2 binary diagram [20] that Gd_2O_3 can be stabilized as the cubic structure up to 1400°C with 2-6 at.% Zr^{4+} doping. Besides, no solid solution behavior is observed between MgO and ZrO_2 below 1400°C [21].

In this work, an innovative strategy is carried out in Gd_2O_3-MgO composite ceramics using 2 at. % Zr as the phase stabilizer of Gd_2O_3. The nitrate-citrate combustion method is used to synthesize the GM/ZGM biphasic nanopowders. A feasible and favorable pressureless pre-sintering in combination with HIP treatment is taken to densify the bulk ceramics. The pressureless shrinkage behavior, phase transition and microstructure evolution of GM and ZGM are investigated systematically with the increasing of pre-sintering temperature. Refractive index, together with transmittance performance, of as-HIPed GM and ZGM bulk ceramics is evaluated experimentally and theoretically as well. The novelty of our present work is ascribed to the distinct pre-sintering profile based on in-situ shrinkage of Gd_2O_3-MgO green bodies with/without Zr doping, which could contribute to a dense microstructure and superior optical performance.

2 Manuscript preparation

2. 1 Synthesis of nanopowders

Equal-volumetric biphasic Gd_2O_3-MgO nanopowders were synthesized by a nitrate-citrate combustion method. $Gd(NO_3)_3{\cdot}6H_2O$ (99.99%, Shanghai Heli Rare Earth Materials Co., LTD, China), $Mg(NO_3)_2{\cdot}6H_2O$, $Zr(NO_3)_4{\cdot}5H_2O$, citric acid monohydrate and ethylene glycol (Sinopharm Chemical Reagent Co., Ltd., AR, Shanghai, China) were used as raw materials. The sol-gel procedure was adapted from the literature [22]. The molar ratio of citric acid to nitrate was 0.20, and the molar ratio of ethylene glycol to citric acid was 0.5. The Zr-doped GM nanopowders were synthesized with 2

mol.% $Zr(NO_3)_4 \cdot 5H_2O$ addition. The calcination temperature here was 800°C to form the nanopowders. The ball milling step was set continuously at 370 rpm for 24 h in zirconia pots using zirconia media in ethyl alcohol. The ball-to-powder ratio was 5:1.

2. 2 Pre-sintering and HIP treatment

The equal-volumetric biphasic GM and 2 at. % Zr doped ZGM nanopowders were pressed into pellets (Φ20 mm × 8 mm) under 10 MPa. The pellets were cold-isostatic-pressed under 200 MPa for 5 min, followed by the pre-sintering stage in a muffle furnace from 1300-1400°C for 2 h at a heating rate of $1°C \cdot min^{-1}$. A capsule-free HIP was further conducted under 200 MPa in Ar atmosphere at 1300°C for 1 h. The as-HIPed samples were annealed at 1000°C for 24 h in air.

2. 3 Characterization

Before pre-sintering, the shrinkage behavior of pressed pellets were examined. They were put on Al2O3 plates and placed in a real-time observation box furnace (Alcera Suzhou inorganic materials Co., LTD, China) with the heating rate of $3°C \cdot min^{-1}$. Pictures of the pellets were captured for recording the real-time sizes of the green body at every increased degree centigrade from room temperature to 1400°C in air. Phase analysis of the nanopowders and as-sintered ceramics was performed using X-ray diffraction (XRD; Ultima IV diffractometer, Rigaku, Tokyo, Japan) with Cu Kα radiation (λ = 1.5406 Å). The morphologies of nanopowders were observed using ultra-high resolution scanning electron microscopy (SEM; SU 9000, Hitachi, Japan). Measurement of nanoparticle size and grain sizes were obtained from the high-resolution SEM images using the mean linear intercept method via the Nanomeasure software (>100 particles/grains). The specific surface area of the as-synthesized nanopowders was measured by the Brunauer-Emmett-Teller (BET, Autosorb iQ, Anton Paar, GA) method. The average particle diameter was determined from the following Eq. (1) [23]:

$$D_{BET} = 6000/(\rho \bullet S_{BET}) \quad \text{Eq. (1)}$$

where S_{BET} is the specific surface area, ρ is the theoretical density, and D_{BET} is the average particle size. The theoretical density of Zr-doped Gd_2O_3, 6.685 $g \cdot cm^{-3}$, was calculated Rietveld refinement of

its XRD pattern. The theoretical density of composite ceramics was calculated based on the rule of mixing, GM of 5.59 g·cm^{-3} and ZGM of 5.12 g·cm^{-3}. The microstructures of ceramics were observed using scanning electron microscopy (SEM; Magellan 400, FEI, Hillsboro, USA) equipped with energy-dispersive spectroscopy (EDS; Inca, Oxford Instrument, UK). Measurements of nanopaticle size and grain sizes were obtained from the SEM images using the mean linear intercept method. The bulk densities of as-sintered ceramics were measured by the Archimedes method. For transmission electron microscopy (TEM) observation, the disks were first mechanically grounded and cut to a diameter of 3 mm and thickness of approximately 100 μm, respectively. They were then thinned by ion-beam down to a thickness of approximately 50 μm and perforated. The microstructures were observed using TEM (Tecnai G2 F20, FEI Co., Hillsboro, USA) working at an accelerating voltage of 200 kV. Selected area electron diffraction (SAED) data was processed using fast Fourier transformation method (FFT). The grain boundary phase was conducted using high-angle annular dark-field scanning transmission electron microscopy (HAADF-STEM) at 100 kV (Model HB501UX, VG Scientifics, East Greensted, UK), using an EDS spectrometer (EDAX, Ametek, USA). A spot size of 6 was selected, a dimensionless parameter from Tecnai microscope control panel. This means the beam diameter is assumed to be 1 nm corresponding to the spot size and beam current. Fourier transform infrared spectroscopy (FT-IR, 4600, JASCO, Japan) was used to identify the functional groups in the powders in the scan range of 400–4000 cm^{-1}. The transmittance was measured using a transmittance mode of the same facility. The specimen for transmittance measurement was polished on both sides with a final thickness of 1 mm. The refractive indexes (n) of GM and ZGM composite ceramics were measured in the range of 1.5-10 μm using Φ 12 mm × 1 mm disks with the single side polished using an IR variable angle spectroscopic ellipsometer (IR-VASE, J. A. Woollam, Lincoln, NE). The detailed testing procedure is described elsewhere [24].

2. 4 Theoretical transmittance and refractive index calculation

In the Zr-doped Gd_2O_3-MgO composite ceramics, cubic Gd_2O_3 was considered as the matrix and MgO as the scattering grain, the theoretical linear transmittance of samples was calculated according to Rayleigh, Mie scattering theory and Beer-Lambert law, as shown in Eq. (2) [25-27]:

$$T = (1 - R)e^{-Q_{sca}d} = 2n/(n^2 + 1) \cdot e^{-8/3} \cdot (2\pi r/\lambda)^4((n_1{}^2 - n_2{}^2)/(n_1{}^2 + 2n_2{}^2))^2 d \quad \text{.....Eq. (2)}$$

Where T was the theoretical linear transmittance; R was the total reflection coefficient of the ceramic sample; Q_{sca} was the scattering coefficient; d was the sample thickness; r was the radius of the scattered particles; l was the wavelength of the incident light; n_1 was the refractive index of the scattered grain; n_2 was the refractive index of the surrounding medium. n was the refractive index of the sample, and f_v was the volume ratio of the scattering particle. Bruggeman equation was used to inverse calculate the refractive indexes of cubic Zr-doped Gd_2O_3 from that of ZGM composite ceramic. The refractive index n_2 of cubic Zr-doped Gd_2O_3 was acquired from the refractive indices of the biphasic composite ceramics using the Eq. (3) [25]:

$$n^2 = (1 - f_v)n_2{}^2 + f_v n_1{}^2 \quad \text{.....Eq. (3)}$$

The refractive index n_1 of MgO relates to l as follows Eq. (4) [8]:

$$n_1 = 1.7200516 + 0.00561194/(\lambda^2 - 0.028)^2 - 0.0030946\lambda^2 - 0.00000961\lambda^4 \quad \text{.....Eq. (4)}$$

3 Results and discussion

3. 1 Properties of biphasic composite nanopowders

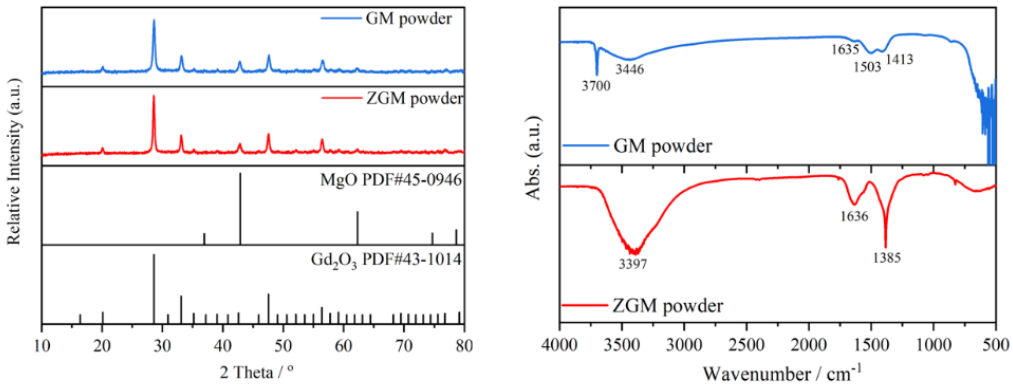

Fig. 1 (a) XRD patterns and (b) FT-IR spectra of calcined GM and ZGM nanopowders.

The XRD pattern (Fig. 1-a) shows that both the calcined GM and ZGM nanopowders are composed of cubic Gd_2O_3 (PDF#43–1014) and MgO (PDF#45–0946) phases, and no impurity phase is observed. The FT-IR spectra of both GM and ZGM nanopowders calcined at 800°C are similar in absorption peaks with predictable results owing to the same synthesis routes: the broad band the stretching vibrations of hydroxyl groups (O–H) at approximately ~3397-3446 cm^{-1}, the carboxylate groups (O–C=O) at 1385-1503 cm^{-1}, and bending of H–O–H at 1635-1636 cm^{-1}[28]. These absorption peaks are possibly formed by the reaction between absorbed moisture and oxides nanoparticles. It has been reported that the residual hydroxyl groups and unreleased carboxylate groups, together with the absorbed moisture, even existed after the calcination at 1100°C. However, it is tricky to balance the sintering activity and purification of these nanoparticles since the grain coarsening had a greater influence on the optical performance.

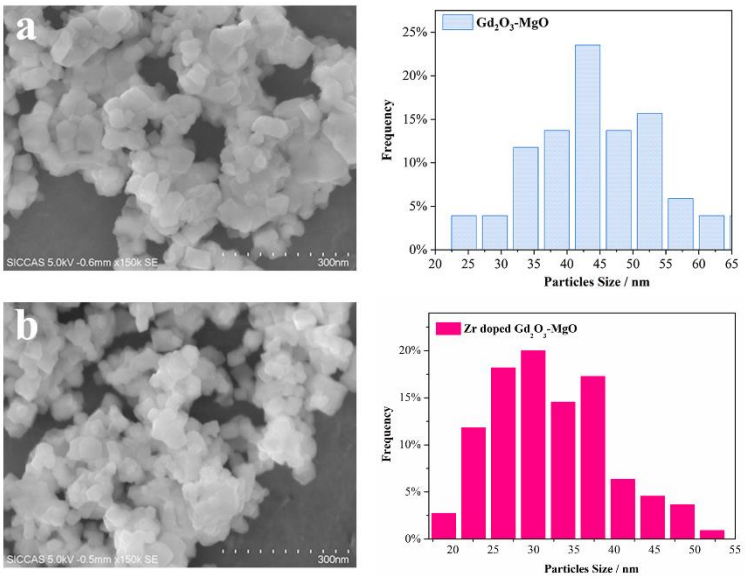

Fig. 2 High resolution secondary electron images and particle size distribution of (a) GM and (b) ZGM nanopowders.

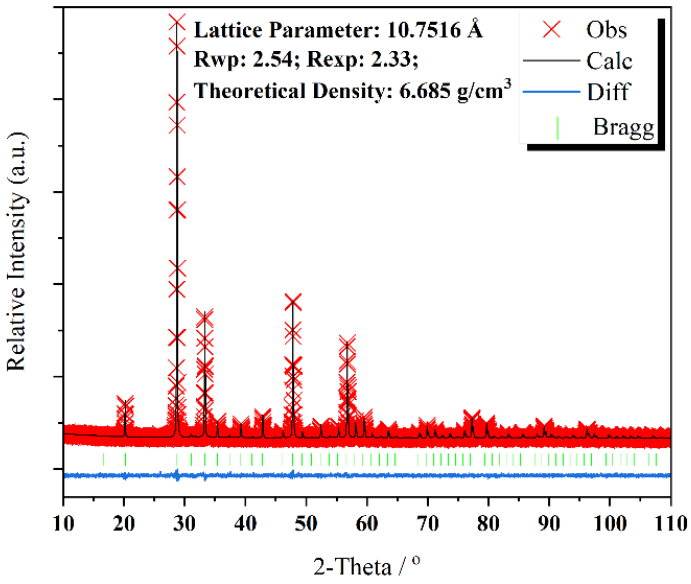

Fig. 3 Rietveld refinement of XRD pattern of Zr-doped Gd_2O_3 nanopowder calcined at 800ºC

The morphologies of the as-synthesized GM and ZGM nanopowders are shown in Fig. 2. Visualized HRSEM was used to analyze the primary particle size distribution of GM and ZGM nanopowders. The frequency of Zr-doped Gd_2O_3-MgO primary particles, increasing in 25-30 nm and disappearing after 55-60 nm particles, implies that the relatively finer particle size was obtained than the undoped one. The main reactions happened between nitrates and citric acid during the sol-gel combustion synthesis, and heat generated that provided driving force of the primary particle growth [29]. It is deduced the doping of Zr doping increased the energy barrier of Gd_2O_3 and led to the smaller particle size [30]. The lattice parameter and theoretical density of Zr-doped Gd_2O_3 pure phase are calculated to be 10.7516 Å and 6.685 $g \cdot cm^{-3}$ via Rietveld refinement of the XRD pattern [31] (Fig. 3). The specific surface areas and crystalline sizes (DBET) of GM and ZGM nanopowders are listed in Table 1. ZGM particles has a mean crystalline size of 43.2 nm, smaller than that of GM (47.3 nm), which shows a good agreement with the measured particle size distribution (Fig. 2). The zirconium ion (0.7200 Å) was reported to occupy the six coordination sites in the cubic Y_2O_3 lattice [32]. It is acceptable that the Zr^{4+} would substitute the similar sites of cubic Gd_2O_3. The doping of Zr^{4+} could bring lots of defects, like oxygen vacancy and oxygen interstitials due to the radius difference, which might influence the mass transport and grain growth rates of Gd_2O_3 phase during sintering. Considering the

charge neutralization on the ZrO_2 doped Gd_2O_3, one interstitial oxygen forms as two Zr atoms replace the lattice sites of Gd, which can be expressed in Kröger-Vink notation as follows [33]:

$$2ZrO_2 \xrightarrow{Gd_2O_3} 2Zr_{Gd}^{\cdot} + O_i'' + 3O_O^X$$

Table 1 Characterizations of GM and ZGM nanopowders

	S_{BET} / m^2/g	D_{BET} / nm
GM	22.7	47.3
ZGM	27.1	43.2

3. 2 Shrinkage features, phase stabilization, and microstructures of optical composite ceramics

The real-time observed shrinkages of the GM and ZGM green bodies are plotted with processing time in Fig. 4-a, c. The pre-sintering shrinkage of the GM green body initiates at approximately 1000°C. The maximum linear shrinkage rate (-0.3 %·min^{-1}) of GM is observed at 1250°C while followed by a declined trend to 1400°C. The phase transition of Gd_2O_3 in GM is verified by XRD patterns at different temperatures (Fig. 4-b). The characteristic XRD peaks of monoclinic Gd_2O_3 (PDF#42–1465) emerges gradually since 1250°C and supersedes the cubic phase peaks (PDF#43–1014) below 1300°C. The drastic final shrinkage of GM green body, 26.0 %, is a profound risk of generating cracks, seeing the inserted picture in Fig. 4-a. While a milder linear shrinkage curve of ZGM green body is observed under the same heating rate. The linear shrinkage curve of ZGM starts below 1000°C and increases more steadily with the processing time, up to -0.2 %·min^{-1} at 1400°C (Fig. 4-c), while that of GM goes like a volatile curve (Fig. 4-a). The XRD patterns of ZGM at different sintering temperatures are essentially unchanged consisting of cubic Gd_2O_3 and MgO. The ZGM sample is obtained intact with a final shrinkage of 26.4 %, inserted in Fig. 4-c. According to the results mentioned above, a modified heating rate of 1°C·min^{-1} is adopted to pre-sinter GM and ZGM green bodies before HIPing. And the cracking of the samples is avoided.

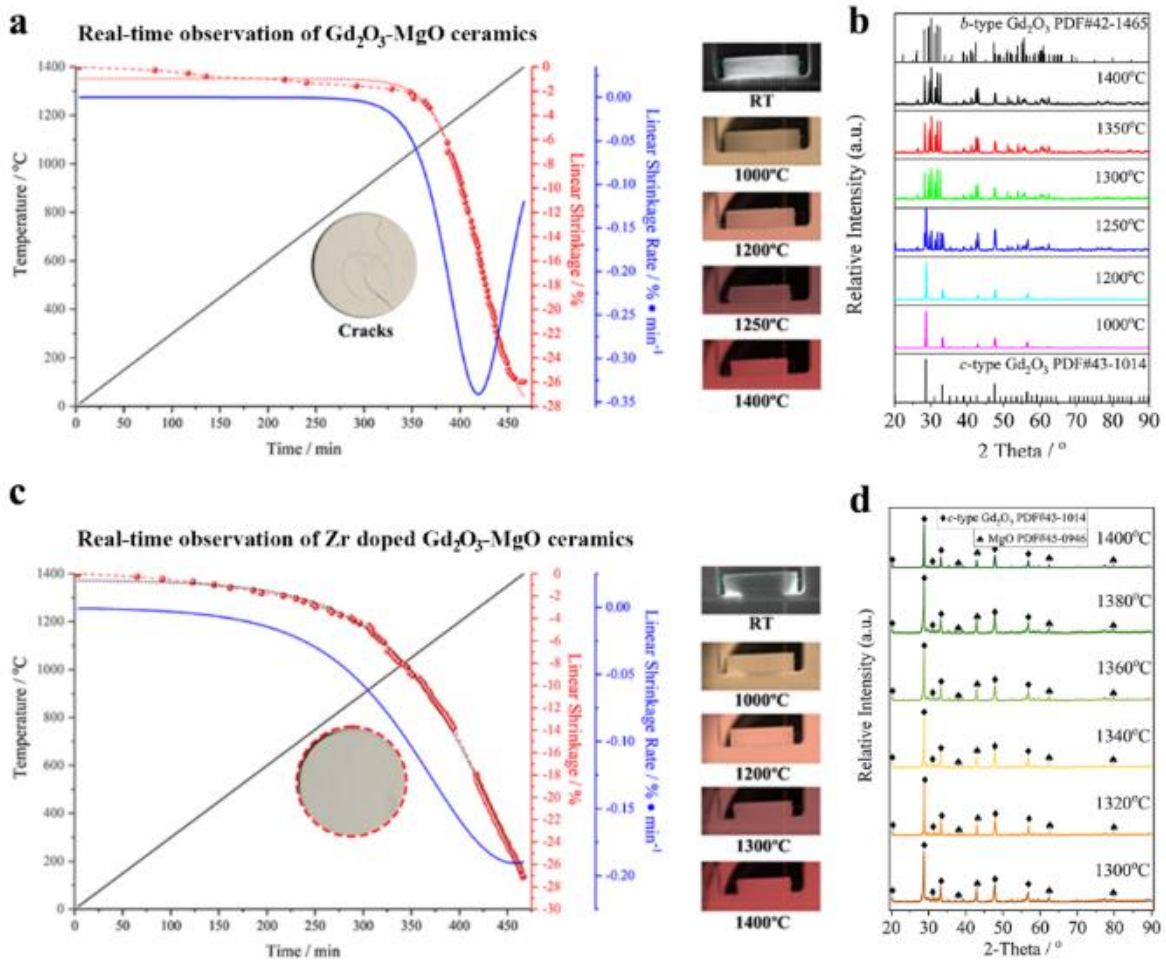

Fig. 4 Real-time observed shrinkage curves and rates of (a) GM and (c) ZGM composite ceramics along with their pictures captured within the furnace; XRD patterns of (b) GM and (d) ZGM bulk ceramics sintered at different temperatures (1300-1400°C).

Table 2 Detailed information of as-HIPed GM and ZGM composite ceramics

Pre-sintering Temperatures / °C	1300	1320	1340	1360	1380	1400
Bulk density of GM g/cm^3	5.50	5.57	5.56	5.55	5.53	5.23
Bulk density of ZGM g/cm^3	4.58	5.02	5.16	5.09	5.04	5.05
Relative density of GM %	98.5	99.7	99.4	99.3	99.0	93.6
Relative density of ZGM %	89.3	98.1	99.9	99.4	98.4	98.6

The detailed information of as-HIPed GM and ZGM bulk ceramics is listed in Table 2. The R.D. of GM increases at first and then decreased from 1300°C to 1400°C with the highest of 99.7% at 1320°C,

while the optimal R.D. 99.9%, of ZGM is obtained with the pre-sintering temperature at 1340°C and an average grain size of Gd_2O_3 of 176 nm.

The post-HIP process is determinative to the elimination of pores without causing the grain growth at lower temperatures than that of the pre-sintering stage. Beforehand, a bulk density of the green body should be pre-sintered to higher than 95%. It can be briefly summarized from Table 2 that higher pre-sintering temperature were necessary to densify the GM bulk ceramics in comparison with that of ZGM.

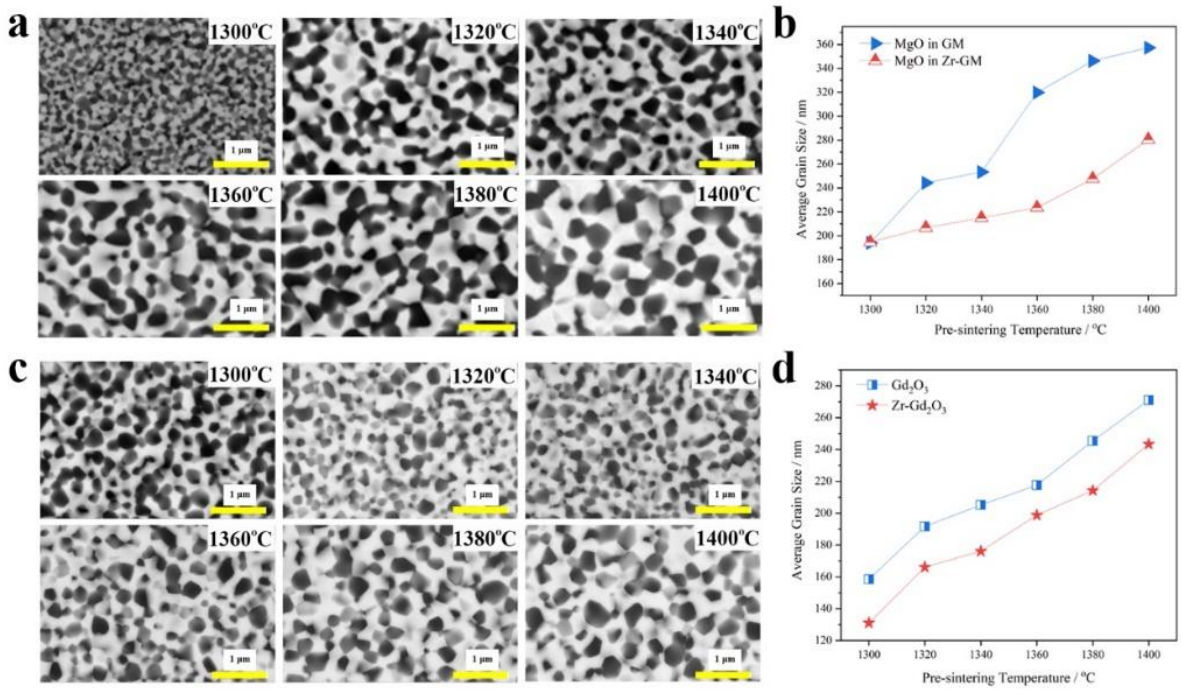

Fig. 5 Backscattered electron images of (a) GM and (c) ZGM composite ceramics (HIPed at 1300°C), along with the average grain sizes of (b) MgO and (d) Gd_2O_3/ Zr-Gd_2O_3 pre-sintered at different temperatures.

The microstructure evolution and grain size variation tendency of GM and ZGM composite ceramics along with the pre-sintering temperature in range of 1300-1400°C are displayed in Fig. 5. Due to the mass contrast in backscattered electron mode, the bright grains are Gd_2O_3/Zr-Gd_2O_3 phase and the dark grains are MgO phase. For GM composite ceramics, the MgO grains grows much faster, from 194 nm at 1300°C to 357 nm at 1400°C (Fig. 5 b), while the average grain size of Gd_2O_3 increases gradually from 158 nm to 271 nm. It is presumed that the abrupt volume shrinkage of Gd_2O_3 provides more space for MgO grains to form the intergranular networking and contributes to the aggravated

grain coarsening of MgO in GM microstructure. No obvious difference between those morphologies of monoclinic and cubic 'Gd_2O_3' are observed. While the MgO grain size of ZGM expands from 195 nm at 1300°C to only 280 nm at 1400°C. As the pre-sintering temperature increases, the average grain size of MgO is bigger than that of Gd_2O_3 phases in both GM and ZGM. It cannot be ignored that the monoclinic Gd_2O_3 phase with higher lattice packing density also grew bigger than that of cubic Gd_2O_3 under the same pre-sintering temperatures within their respective microstructures. The curiosity next is what other influencing factors would drag the grain growth of cubic Gd_2O_3 in ZGM. Zr^{4+} ion is treated as the most effective grain growth inhibitor of RE_2O_3 owing to the possible solute drag effect. Chen et al. [34] reported that the 1 at. % Zr^{4+} dopant decreased the grain boundary mobility of Y_2O_3 during densification process.

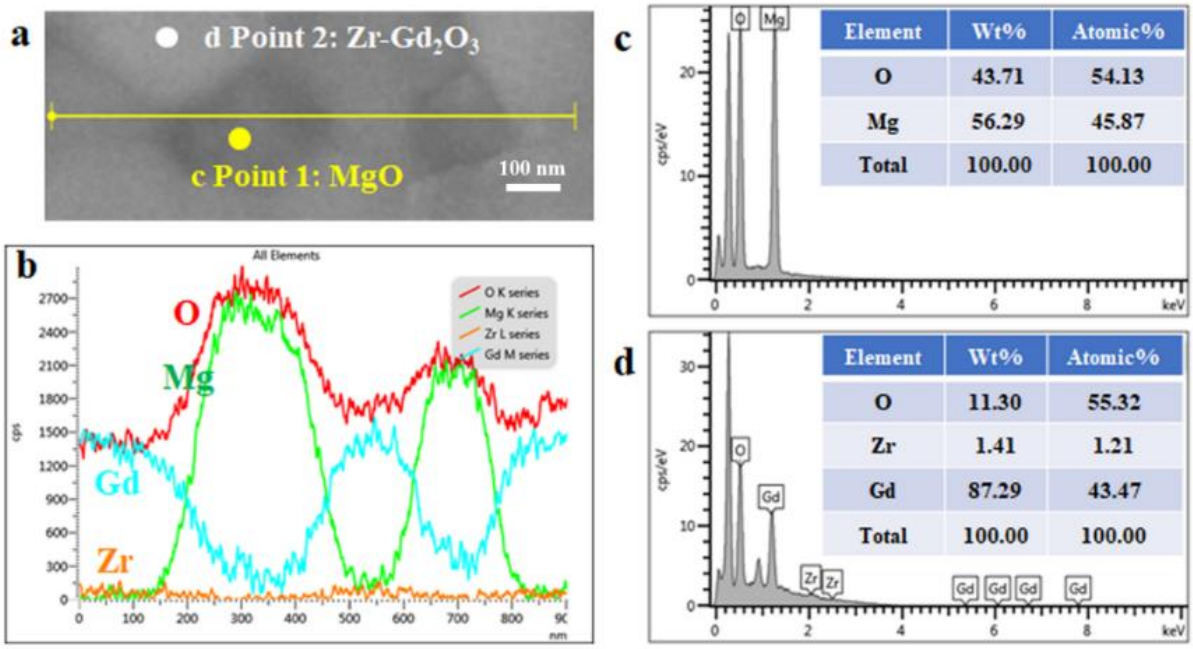

Fig. 6 (a) Magnified SEM of as-HIPed ZGM composite ceramic (pre-sintered at 1340°C, HIPed at 1300°C) with its (b) EDS line scanning and point analysis (c, d).

Further investigation is conducted on the almost fully dense ZGM sample, pre-sintered at 1340°C and followed by HIP at 1300°C. The Zr-doped Gd_2O_3 and MgO grains are distinguished successfully via the EDS line scanning, as shown in Fig. 6-a, b. The MgO phase is identified with no Zr element doping. While about 1.21 at. % of Zr is confirmed to be doped within the Gd_2O_3 grain based on the

EDS point analysis (Fig. 7- d). Detailed investigation on the distribution of Zr element in the microstructure of Zr-doped Gd_2O_3-MgO composite ceramics is carried out using high-resolution TEM technique.

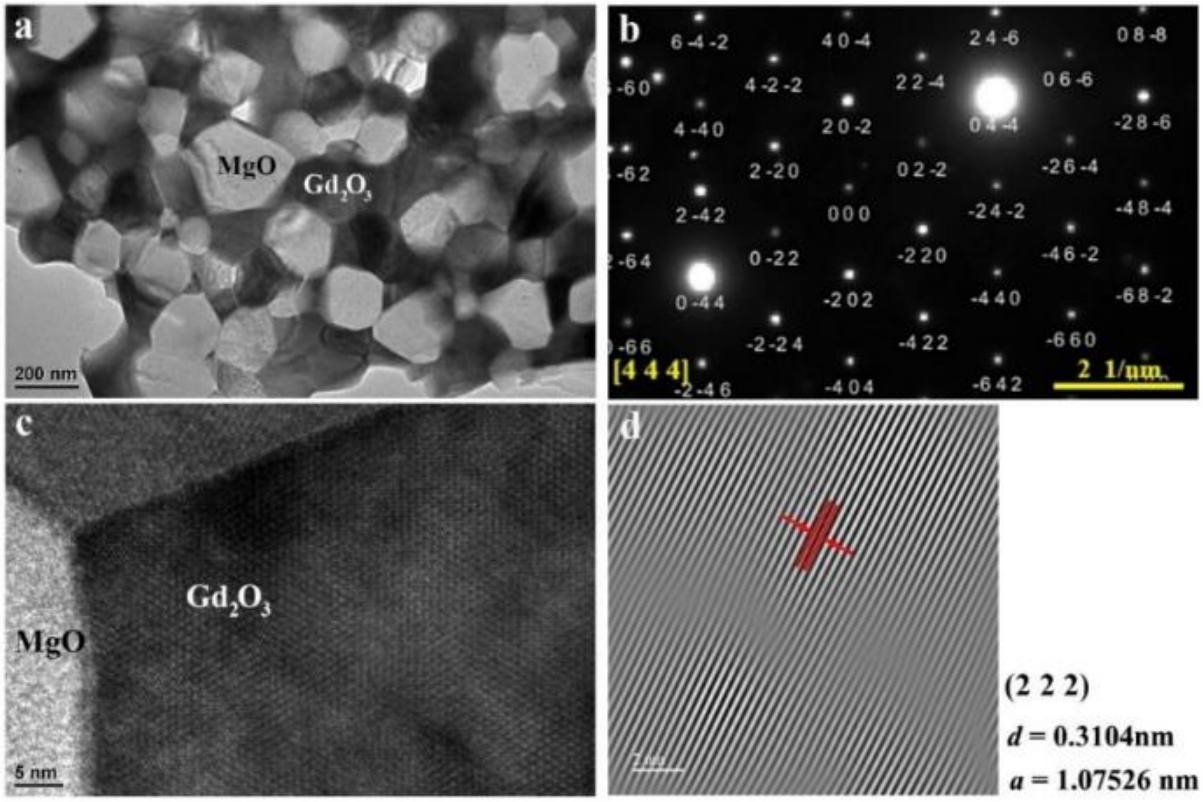

Fig. 7 (a) TEM image of as-HIPed ZGM composite ceramic (pre-sintered at 1340°C, HIPed at 1300°C); (b) SAED, (c) HRTEM and (d) inverse FFT images of Gd_2O_3 grain.

The TEM image of the ZGM sample is shown in Fig. 7. The distribution of the two phases is very uniform (Fig. 7-a). The dark phase, marked with Gd_2O_3, has a crystallographic zone axis of [4 4 4] and is verified to be cubic phase by SAED in Fig. 7-b. The bright phase is MgO. The grain boundary between Gd_2O_3 and MgO is checked via HRTEM analysis, and no impurity phase is observed (Fig. 7-c). The lattice parameter of Zr-doped Gd_2O_3 phase is calculated to be 10.7526 Å using inverse FFT, which is quite close to the result obtained by Rietveld refinement.

The Gd_2O_3 and MgO phases are more visible as bright and dark regions in the STEM mode that is sensitive to atomic number contrast (Fig. 8-a). Additionally, the Zr element distribution is checked using the HAADF-STEM-EDS. Conversely, EDS mapping is conducted in the red box area in Fig. 8-

a and shown in Fig. 8-b, c, d. The Gd element distributed homogenously, while a slight nonuniformity is found in the Zr element mapping. The area of the red box for HAADF-STEM-EDS mapping was 124nm x105 nm. EDS mapping scan frame was composed of 20 x 17 pixels. As mentioned in the experimental part, each EDS pixel (6.2nm x 6.2nm) of Gd or Zr was acquired after the 1nm-size beam dwelling for 1000ms at the position. The results in Fig. 8 provide high precision in distinguishing the distribution of Gd and Zr. As shown in Fig. 8 c and d, the Gd and Zr element mapping are not well overlapped and the Zr element segregates mostly at Gd_2O_3 grain boundaries. Hence, it is confirmed that the evident segregation of Zr appears along the grain boundary of Gd_2O_3 grains. Ostwald ripening is used to explain the mechanism of the grain growth and establishes on the effective adjacency degree of grains. In the case of our study, the grain growth of Gd_2O_3 is not only inhibited by the MgO phase, but also threatened by the Zr segregation along grain boundaries. The synergistic effect, from both the Zener pinning and doping element segregation, eventually leads to a finer grain size of Gd_2O_3.

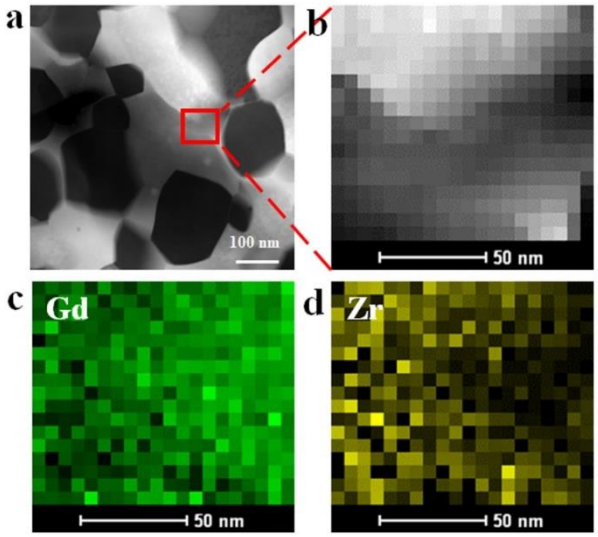

Fig. 8 (a) HAADF-STEM image of as-HIPed ZGM ceramic; (b, c, d) EDS element mapping from the red box area in (a).

3. 3 Infrared transmittance and refractive index of optical composite ceramics

As shown in Fig. 9, the transmittances of both GM and ZGM increases along with the raising in pre-sintering temperatures, which leads to the increase in their relative densities (Table 2). The GM composite ceramic, which was pre-sintered at 1320°C, has the relatively higher transmittance of

60.5%-82.0% at 3-5 μm among those with different pre-sintering temperatures. The poor MWIR transmittance of GM ceramics in 3-5 μm is mainly caused by large average grain sizes and residual pores. While the ZGM ceramic pre-sintered at 1340°C exhibits a better performance in transmittance of 78.3%-85.6% at 3-5 μm with the highest value of 86.4% at 5.5 μm. No obvious absorption peaks from the stretching vibrations of carboxylate (~ 7 μm) and -OH (~ 2.5-3.5 μm) groups are observed. Although the cut-off in short wavelength is negatively associated with the scattering grain sizes, results here seemed not strictly following. The leading scattering factor is got boiled down to the residual pore since their scattering grain sizes are similar.

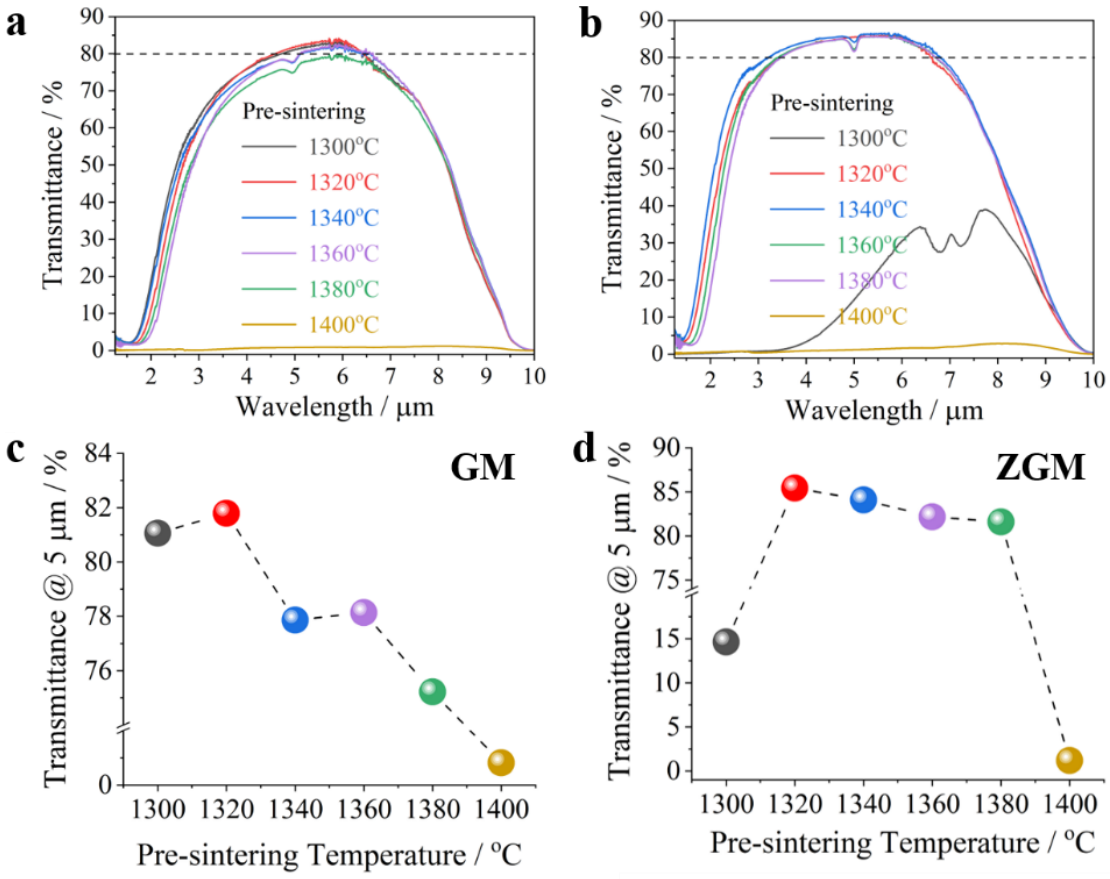

Fig. 9 Transmittance of (a) GM and (b) ZGM ceramics pre-sintered at temperatures from 1300 to 1400°C, followed by the post-HIP at 1300°C; transmittance at 5 μm of as-HIPed (c) GM and (d) ZGM. The thickness of samples was 1 mm.

It is worth noting that a sharp absorption peak appeared at ~ 5 μm among most of dense GM and ZGM samples except samples pre-sintered at 1320°C in Fig. 9-a, b. Both the specific transmittance

values at 5 μm from series of GM and ZGM samples shows a parabolic distribution when plotting with pre-sintering temperatures (Fig. 9-c, d). The highest transmittance values of 5 μm appears coincidentally on both the samples pre-sintered at 1320°C: 81.2% for GM and 85.4% for ZGM. This result can be explained by the trapped CO gas in the closed pores by reduction reaction of residual carbon during densification. The impact of CO gas absorption signal affects the transmittance performance differed with the pre-sintering temperatures variation [35]. This phenomenon sets links between the reduction reaction in nitrate-citrate gel derived nanopowders and the shrinkage behavior during sintering. An inferential conclusion is therefore proposed that the escaping channels of CO were gradually narrowed with the pre-sintering temperature increasing. Although the transmittance performance differs slightly, trivial absorption peaks should be further optimized in perspective of advanced densification technology.

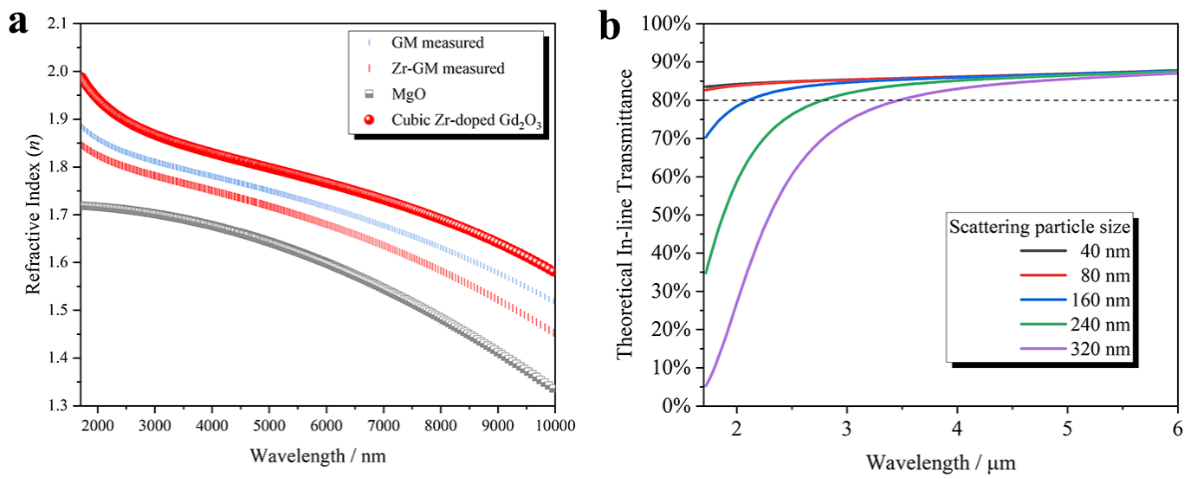

Fig. 10 (a) Measured refractive index of GM and ZGM ceramics and deductive refractive index of cubic Zr-doped Gd_2O_3. The thickness of samples was 1 mm. (b) calculated theoretical in-line transmittance of Zr-doped Gd_2O_3-MgO with various MgO scattering particle sizes in the range of 1-6 μm.

The refractive indexes of the bulk composite ceramics, cubic Zr-Gd_2O_3 and MgO phases are plotted in a parabolic manner with the wavelength in the range of 1.5-10 μm, as shown in Fig. 10-a. The measured n of ZGM sample shows a decreasing trend from 1.78 at 3 μm to 1.72 at 5 μm, and the n of GM sample exhibits the relatively higher values from 1.81 to 1.75 in the range of 3-5 μm. The n of cubic structured Zr-doped Gd_2O_3 varies from 1.87 at 3 μm to 1.80 at 5 μm, which is smaller than those

of monoclinic structured Gd_2O_3 [36, 37]. It is speculated that the difference in n was mainly attributed to the lattice environment change of Gd_2O_3. As shown in Fig. 10-b, the transmittance of 1:1 Zr-doped Gd_2O_3-MgO composite ceramics is calculated in the MWIR range by considering Mie scattering theory and Beer-Lambert equation. The critical scattering grain size of MgO and cubic Zr-doped Gd_2O_3 should be tailored below ~240 nm to achieve a MWIR transparent condition (>80%) in the range of 3-5 μm. By contrast, the measured transmittance of dense ZGM ceramic pre-sintered at 1340°C possesses the relatively poor transmittance value of 78.3% at 3 μm with the mean grain size (MGS) finer than the critical size, 176 nm Zr-Gd_2O_3 and 215 nm MgO. In this study, the transmittance in MWIR range is mainly dominated by scattering source, such as the Zr-Gd_2O_3/MgO interface, residual pores, and inhomogeneous distribution of Zr element, rather than the crystal structures of Gd_2O_3.

4 Conclusions

Zr stabilized the cubic crystalline structured Gd_2O_3 hybrid with MgO composite ceramics are densified using the nitrate-citrate gel derived biphasic nanopowders as starting materials. Main results are following:

(1)The lattice parameter of Zr-doped Gd_2O_3 are calculated to be 10.7516 Å by Rietveld refinement. The D_{BET} of ZGM nanopowders (43.2 nm) is slightly smaller than that of GM nanopowders (47.3 nm). The Zr-doped Gd_2O_3 can be stabilized as the cubic structure up to 1400°C.

(2)The pressureless shrinkage of ZGM green body proceeds more steadily up to 1400°C, and the finer grain sizes of ZGM are contributed by both the pinning effect from MgO phase and the Zr-segregation along grain boundaries.

(3)The ZGM samples, pre-sintering at 1340°C and HIP at 1300°C (R.D. 99.9%, MGS of Zr-Gd_2O_3 176 nm, MGS of MgO 215 nm), exhibit superior transmittance of 78.3%-85.6% at 3-5 μm with the highest value of 86.4% at 5.5 μm. It is speculated that the trapped CO gas affected the transmittance values at 5 μm.

Acknowledgements

This work was supported by the director of transparent ceramics research center of Shanghai Institute of Ceramics, Chinese Academy of Sciences (Director's Fund 2021), National Natural Science Foundation of China (No. 52272076), and Shanghai Sailing Program (22YF1455700).

References

[1] A. Ikesue, Processing of Ceramics: Breakthroughs in Optical Materials, John Wiley & Sons, 2021.

[2] M. Nofar, H.M. Hosseini, H. Shivaee, The dependency of optical properties on density for hot pressed MgF_2, Infrared Phys. Technol. 51 (2008) 546-549.

[3] Y. Sun, S. Shimai, X. Peng, G. Zhou, H. Kamiya, S. Wang, Fabrication of transparent Y_2O_3 ceramics via aqueous gelcasting, Ceram. Int. 40 (2014) 8841-8845.

[4] W. Luo, R. Xie, M. Ivanov, Y. Pan, H. Kou, J. Li, Effects of LiF on the microstructure and optical properties of hot-pressed $MgAl_2O_4$ ceramics, Ceram. Int. 43 (2017) 6891-6897.

[5] J. Li, B. Zhang, R. Tian, X. Mao, J. Zhang, S. Wang, Hot isostatic pressing of transparent AlON ceramics assisted by dissolution of gas inclusions, J. Eur. Ceram. Soc. 41 (2021) 4327-4336.

[6] D.A. Permin, M.S. Boldin, A.V. Belyaev, S.S. Balabanov, V.A. Koshkin, A.A. Murashov, I.V. Ladenkov, E.A. Lantsev, K.E. Smetanina, N.M. Khamaletdinova, IR-transparent MgO-Gd_2O_3 composite ceramics produced by self-propagating high-temperature synthesis and spark plasma sintering, J. Adv. Ceram. 10 (2021) 237-246.

[7] N. Jiang, R.-j. Xie, Q. Liu, J. Li, Fabrication of sub-micrometer MgO transparent ceramics by spark plasma sintering, J. Eur. Ceram. Soc. 37 (2017) 4947-4953.

[8] J. Al-Sharab, R. Sadangi, V. Shukla, B. Kear, J. Bentley, Characterization of Y_2O_3-MgO Nanostructures Prepared by Argon Shrouded-Plasma Spraying, Microscopy 14 (2008) 310-311.

[9] Z. Fang, H. Wang, Densification and grain growth during sintering of nanosized particles, Inter. Mater. Rev. 53 (2008) 326-352.

[10] D.C. Harris, L.R. Cambrea, L.F. Johnson, R.T. Seaver, M. Baronowski, R. Gentilman, C. Scott

Nordahl, T. Gattuso, S. Silberstein, P. Rogan, Properties of an Infrared-Transparent MgO:Y_2O_3 Nanocomposite, J. Am. Ceram. Soc. 96 (2013) 3828-3835.

[11] L. Liu, K. Morita, T.S. Suzuki, B.-N. Kim, Evolution of microstructure, mechanical, and optical properties of Y_2O_3-MgO nanocomposites fabricated by high pressure spark plasma sintering, J. Eur. Ceram. Soc. 40 (2020) 4547-4555.

[12] L. Liu, K. Morita, T.S. Suzuki, B.-N. Kim, Effect of volume ratio on optical and mechanical properties of Y_2O_3-MgO composites fabricated by spark-plasma-sintering process, J. Eur. Ceram. Soc. 41 (2021) 2096-2105.

[13] N. Wu, X. Li, J.G. Li, Q. Zhu, X. Sun, Fabrication of Gd_2O_3-MgO nanocomposite optical ceramics with varied crystallographic modifications of Gd_2O_3 constituent, J. Am. Ceram. Soc. 101 (2018) 4887-4891.

[14] N. Wu, X. Li, M. Zhang, Y. Ren, Q. Zhu, H. Peng, H. Ru, X. Sun, Synthesis of nanopowders with low agglomeration by elaborating Φ values for producing Gd_2O_3-MgO nanocomposites with extremely fine grain sizes and high mid-infrared transparency, J. Eur. Ceram. Soc. 41 (2021) 2898-2907.

[15] K. Morita, B.N. Kim, H. Yoshida, K. Hiraga, Y. Sakka, Influence of spark plasma sintering (SPS) conditions on transmission of $MgAl_2O_4$ spinel, J. Am. Ceram. Soc. 98 (2015) 378-385.

[16] S.-M. Yong, D.H. Choi, K. Lee, S.-Y. Ko, D.-I. Cheong, Y.-J. Park, S.-I. Go, Study on carbon contamination and carboxylate group formation in Y_2O_3-MgO nanocomposites fabricated by spark plasma sintering, J. Eur. Ceram. Soc. 40 (2020) 847-851.

[17] J.-M. Kim, H.-N. Kim, Y.-J. Park, J.-W. Ko, J.-W. Lee, H.-D. Kim, Microstructure and optical properties of transparent $MgAl_2O_4$ prepared by Ca-infiltrated slip-casting and sinter-HIP process, J. Eur. Ceram. Soc. 36 (2016) 2027-2034.

[18] S. Wang, J. Zhang, D. Luo, F. Gu, D. Tang, Z. Dong, G. Tan, W. Que, T. Zhang, S. Li, Transparent ceramics: Processing, materials and applications, Progress in solid state chemistry 41(1-2) (2013) 20-

54.

[19] F. Zhang, M. Lang, J. Wang, U. Becker, R. Ewing, Structural phase transitions of cubic Gd_2O_3 at high pressures, Phy. Rev. B 78 (2008) 064114.

[20] T.D. N.B. Lazar Rokhlin, Natalia Kolchugina, Oleksandr Dovbenko and MSIT, Phase diagram of the ZrO_2-Gd_2O_3 system, https://materials.springer.com/msi/phase-diagram/docs/sm_msi_r_10_010853_01_full_LnkDia3.

[21] D. Yong, J. Zhanpeng, Optimization and calculation of the ZrO_2-MgO system, Calphad 15 (1991) 59-68.

[22] Z. Shen, J. Xie, K. Qian, Q. Zhu, X. Mao, M. Feng, B. Jiang, L. Zhang, J. Fan, Preparation and study of the mechanical and optical properties of infrared transparent Y_2O_3–MgO composite ceramics, J. Am. Ceram. Soc. 104 (2021) 6335-6344.

[23] J.-G. Li, T. Ikegami, T. Mori, Fabrication of transparent Sc_2O_3 ceramics with powders thermally pyrolyzed from sulfate, J. Mater. Res. 18 (2003) 1816-1822.

[24] Y. Yang, Z. Yang, P. Lucas, Y. Wang, Z. Yang, A. Yang, B. Zhang, H. Tao, Composition dependence of physical and optical properties in Ge-As-S chalcogenide glasses, J. Non-Cryst. Solids 440 (2016) 38-42.

[25] S. Liu, M.D. Islam, Z. Ku, D.A. Boyd, Y. Zhong, A.M. Urbas, E. Smith, J. Derov, V.Q. Nguyen, W. Kim, Novel computational design of high refractive index nanocomposites and effective refractive index tuning based on nanoparticle morphology effect, Composites Part B: Engineering 223 (2021) 109128.

[26] R. Apetz, M.P. Van Bruggen, Transparent alumina: a light-scattering model, J. Am. Ceram. Soc. 86(3) (2003) 480-486.

[27] L. Qing, Study on the Light Transmission Mechanism and Scattering Models of Transparent Ceramics, Ph.D. Thesis. Wuhan(China), Central China Normal University, 2011.

[28] J. Xie, X. Mao, X. Li, B. Jiang, L. Zhang, Influence of moisture absorption on the synthesis and

properties of Y_2O_3–MgO nanocomposites, Ceram. Int. 43(1) (2017) 40-44.

[29] J. Wang, D. Chen, E.H. Jordan, M. Gell, Infrared-Transparent Y_2O_3–MgO Nanocomposites Using Sol–Gel Combustion Synthesized Powder, J. Am. Ceram. Soc. 93(11) (2010) 3535-3538.

[30] R. Zhang, A. Khalizov, L. Wang, M. Hu, W. Xu, Nucleation and growth of nanoparticles in the atmosphere, Chem. Rev. 112(3) (2012) 1957-2011.

[31] J.E. Post, D.L. Bish, Rietveld refinement of crystal structures using powder X-ray diffraction data, Modern powder diffraction 20 (1989) 277-308.

[32] X. Li, X. Mao, M. Feng, J. Xie, B. Jiang, L. Zhang, Optical absorption and mechanism of vacuum-sintered ZrO_2-doped Y_2O_3 ceramics, J. Eur. Ceram. Soc. 36 (2016) 4181-4184.

[33] Y. Katayama, H. Tomimoto, J. Ueda, S. Tanabe, Modulation of the optical properties of Pr^{3+}-doped Y_2O_3 ceramics by Zr doping, J. Ceram. Soc. Jap. 122 (2014) 89-92.

[34] P.L. Chen, I.W. Chen, Grain boundary mobility in Y_2O_3: defect mechanism and dopant effects, J. Am. Ceram. Soc. 79 (1996) 1801-1809.

[35] H.J. Ma, J.H. Kong, D.K. Kim, Insight into the scavenger effect of LiF on extinction of a carboxylate group for mid-infrared transparent Y_2O_3- MgO nanocomposite, Scripta Mater. 187 (2020) 37-42.

[36] O. Medenbach, D. Dettmar, R. Shannon, R. Fischer, W. Yen, Refractive index and optical dispersion of rare earth oxides using a small-prism technique, J Opt. A 3 (2001) 174.

[37] Y.A. Kuznetsova, A. Zatsepin, N. Gavrilov, The high refractive index of Gd_2O_3 thin films obtained by magnetron sputtering, Opt. Mater. 120 (2021) 111382.